



Static recrystallisation and corrosion behavior of a hot-rolled AZ31 magnesium alloy

Samia Tighiouaret, Abdelkader Hanna, Hiba Azzeddine, Lyacine Rabahi, Achour Dakhouche, François Brisset, Anne-Laure Helbert, Thierry Baudin, Djamel Bradai

► To cite this version:

Samia Tighiouaret, Abdelkader Hanna, Hiba Azzeddine, Lyacine Rabahi, Achour Dakhouche, et al.. Static recrystallisation and corrosion behavior of a hot-rolled AZ31 magnesium alloy. 2020. hal-03048866

HAL Id: hal-03048866

<https://hal.science/hal-03048866>

Preprint submitted on 9 Dec 2020

HAL is a multi-disciplinary open access archive for the deposit and dissemination of scientific research documents, whether they are published or not. The documents may come from teaching and research institutions in France or abroad, or from public or private research centers.

L'archive ouverte pluridisciplinaire **HAL**, est destinée au dépôt et à la diffusion de documents scientifiques de niveau recherche, publiés ou non, émanant des établissements d'enseignement et de recherche français ou étrangers, des laboratoires publics ou privés.

Static recrystallisation and corrosion behavior of a hot-rolled AZ31 magnesium alloy

Samia Tighiouaret¹, Abdelkader Hanna¹, Hiba Azzeddine^{1*}, Lyacine Rabahi^{2,3}, Achour Dakhouche⁴, François Brisset⁵, Anne-Laure Helbert⁵, Thierry Baudin⁵, Djamel Bradai²

¹ Department of Physics, University of Mohamed Boudiaf, M'sila, 28000, Algeria

² Laboratory of Materials Physics, Faculty of Physics, University of Sciences and Technology - Houari Boumediene (U.S.T.H.B.), P.O. Box 32, El-Alia, Bab-Ezzouar, DZ-16111, Algiers, Algeria

³ Research Center in Industrial Technologies CRTI. P.O. Box 64, Cheraga, Algiers, 16014, Algeria

⁴ Inorganic Materials Laboratory, Department of chemistry, Faculty of Sciences, University of Mohamed Boudiaf, M'sila, 28000, Algeria

⁵ Université Paris-Saclay, CNRS, Institut de chimie moléculaire et des matériaux d'Orsay, 91405, Orsay, France

* Corresponding author: Dr. Hiba Azzeddine, email: hiba.azzeddine@univ-msila.dz

Abstract

The microstructure and texture of an AZ31 alloy were investigated after hot rolling at 350°C to achieve low, medium and high strain (i.e., 20%, 50% and 85% thickness reduction, respectively) and subsequent annealing at 350°C for 2, 10 and 60 min using electron backscatter diffraction. The effect of hot rolling and subsequent static recrystallisation on corrosion behavior in seawater was also evaluated using electrochemical tests. At low strain, the microstructure was characterised by the absence of twinning, mainly due to the prior deformation state of the as-received alloy. However, various modes of twinning were observed at medium strain. At high strain, the dynamic recrystallisation process resulted in a microstructure with a typical basal texture. The results demonstrate that twins are responsible for the deviation of {0002} basal poles from normal towards the transversal direction. Annealing at 350°C for up to 60 min led to normal grain growth in all the samples. In medium and highly strained samples, the deformation texture was retained, while the low strain sample underwent noticeable changes due to the absence of dynamic recrystallisation. A synergetic effect of grain refinement and texture weakening was responsible for the alloy's enhanced corrosion resistance.

Keywords: AZ31 alloy; Corrosion; Dynamic recrystallisation; Static recrystallisation; rolling

1. Introduction

One of the greatest challenges in the automotive industry is reducing vehicle mass to increase fuel efficiency and global performance, as well as reduce environmental impacts [1]. The low density of magnesium, which is 36% and 78% lighter than aluminum and steel, respectively, makes it the most promising candidate for this purpose [2]. However, traditionally, Mg-based alloys comprise less than 1% of a vehicle's weight [3]. The commercial use of Mg-based alloy sheets is limited, as their hexagonal close pack (HCP) structure and the formation of a strong basal texture [4, 5] at lower temperatures result in low formability. Furthermore, Mg-based alloys generally suffer from relatively poor corrosion resistance due to their low standard electrochemical potential, which restricts their use in a variety of applications [6].

Modifying the microstructure of Mg-based alloys by thermo-mechanical processing is considered an effective way to significantly improve formability and control corrosion behavior by reducing mechanical anisotropy. Usually, this is achieved by promoting the activation of non-basal slip modes, controlling the activation of mechanical twinning, precipitation strengthening and the occurrence of the dynamic recrystallisation (DRX) process [7-15]. Several DRX mechanisms have been proposed to explain the resulting microstructure and texture, such as twin-induced dynamic recrystallisation (TDRX) [16], rotational dynamic recrystallisation (RDRX) [17] and strain-induced boundary migration (SIBM) [17]. Furthermore, the microstructure of a deformed alloy is unstable due to the presence of deformation-induced defects, such as dislocations; hence, the material cannot be used as a final product. Therefore, post-deformation annealing treatments are often performed on processed alloys to reach a more stable state by static recrystallisation and grain growth phenomena [18].

Numerous studies involving the evolution of the microstructure and texture of Mg-based alloys during thermo-mechanical processing and subsequent annealing treatments are reported in the literature [5, 12, 19-32]. However, the mechanisms responsible for microstructure and texture evolution during deformation processing and recrystallisation treatment are not well understood, and some reports provide controversial results. Some studies indicate that the occurrence of twin-induced dynamic recrystallisation characterised by the formation of recrystallised grains inside the twins might develop a texture different from the deformation one [33, 34]. Other studies demonstrate that the orientations of dynamically recrystallised grains are the same than those of the host twins [35, 36]. Additionally, abnormal grain growth phenomena were observed in a hot-rolled AZ31 alloy during long (up to 3 days)

annealing at temperatures of 260–450°C [23]. However, they were not observed in an AZ31 alloy after hot-rolling and subsequent annealing at 450°C for 7 days [37].

In addition to the nature of alloying-addition elements, many experimental parameters might control the occurrence of these mechanisms and, therefore, affect the alloy's final microstructure and texture, such as the deformation conditions (i.e., the deformation temperature, strain, and strain rate) or annealing treatment (i.e., the temperature and duration). Consequently, controlling the effect of such parameters on Mg-based alloys' performance could greatly improve the design of Mg-based alloys for large industrial applications.

Thus, the present investigation explores the effects of strain levels on the evolution of the microstructure and texture of an AZ31 (Mg-3Al-1Zn, wt.%) alloy. The AZ31 alloy was hot-rolled at 350°C to achieve low, medium and high strain (i.e., 20%, 50% and 85% thickness reduction, respectively) and subsequent annealing treatment at 350°C for 2–60 min. Furthermore, the AZ31 alloy's corrosion behavior in seawater collected from the Mediterranean Sea was evaluated. Previously, a limited investigation of the effect of hot-rolling on the corrosion behavior of the same AZ31 alloy in 0.9% NaCl (wt.%) solution was reported [38]. Hence, the present paper aims to investigate the corrosion behavior of an AZ31 alloy with microstructural and textural variation in seawater under different thermo-mechanical conditions, including recrystallisation and grain growth phenomena.

2. Experimental procedure

2.1. Material

Sheets of an AZ31 alloy with a thickness of 2.2 mm were kindly supplied by Magnesium Innovations Center (MagIC) in Germany. Detailed information regarding the sheets' chemical composition is presented in Table 1. The rolling experiments were conducted at a nominal rolling temperature of 350°C. The total reductions in thickness were 20%, 50% and 85%, with a 10% reduction per pass. After each rolling step, the rolled samples were returned to the furnace and reheated for 10 min to regain the rolling temperature. After the final rolling pass, the samples were quenched in water. The hot-rolled AZ31 samples were then annealed at 350°C for 2, 10 and 60 min in a radiation furnace, followed by water quenching.

2.2. Microstructural and textural observations

The microstructures of the as-received, hot-rolled and annealed samples were investigated using electron backscatter diffraction (EBSD) in the RD-TD plane after

mechanical and ionic polishing using a Gatan PECS II system at a high voltage of 5 kV for 15 min, where RD and TD denote the rolling and transversal directions, respectively. The observations were carried out using a FEG-SEM SUPRA 55 VP scanning electron microscope operating at 20 kV. EBSD data acquisition and analysis were undertaken using an TSL orientation imaging microscopy system and OIMTM software. The scanned areas were $80 \times 80 \mu\text{m}^2$ with a $0.2 \mu\text{m}$ step size, and the grain-size data were obtained using a grain tolerance angle of 5° . The minimum grain size was set at 5 pixels. All datum points with a confidence index lower than 0.05 were excluded from the analysis; the confidence index quantifies the reliability of the indexed pattern [39]. Quantitative texture analysis was carried out by calculating the orientation distribution function (ODF) using MTEX software [40]. The ODF was calculated using the harmonic method ($L = 22$), and each orientation was modelled using a Gaussian function with a half-width of 5° .

2.3. Vickers microhardness

A Shimadzu type HMV-2 tester was used to measure the Vickers microhardness (Hv) on the RD-TD plane of the samples by using a load of 100 g ($\text{HV}_{0.1}$) and a dwell time of 10 s. The average microhardness values were calculated from at least five indentations.

2.4. Electrochemical testing

Electrochemical tests were conducted using an Autolab PGSTAT302N workstation and a standard three-electrode cell. The samples were embedded in an epoxy resin to isolate a 1 cm^2 area from the non-studied surfaces. The open-circuit potential (OCP) was measured for at least 60 min for all samples in a seawater solution (collected from the Mediterranean Sea) at ambient temperature. Impedance measurements were subsequently performed using a sinusoidal potential signal with an amplitude of 10 mV in the frequency range of 10^{-2} – 10^5 Hz. Experimental curves were fitted using Zview software. As-received sample was immersed in seawater for 3 h, followed by corrosion morphology analysis using a scanning electron microscope (SEM, FEG-SEM ZEISS Gemini) equipped with an energy dispersive spectrometry (EDS) system in backscatter (BSE) mode at 15 kV.

3. Results

3.1. Microstructure and texture of the as-received AZ31 alloy

Figs. 1a and 1b show the microstructure of the as-received AZ31 alloy in terms of orientation imaging micrographs in an inverse pole figure (ND-IPF) mode and grain

orientation spread (GOS) maps. The white and black lines in the ND-IPF map are ascribed to low-angle grain boundaries (LAGBs, $2-15^\circ$) and high-angle grain boundaries (HAGBs, $>15^\circ$), respectively. The GOS approach implemented in OIM software allows the net separation of recrystallised and deformed grains. The GOS parameter is defined as the average deviation between the orientation of each point in the grain and the average orientation of the grain [41]. Usually, the grains were considered recrystallised in Mg-based alloys if the GOS parameter varied between 1° and 2° [42-44]. As shown, most of the grains were deformed and contained a high amount of low-angle grain boundaries (LAGBs). In addition, some deformation twins could be observed in the microstructure. The black zones present in the microstructure indicate some highly deformed areas of the sample. The average grain size was found to be $16.1 \pm 0.6 \mu\text{m}$. The recalculated $\{0002\}$ pole figure shown in Fig. 1c indicates that the as-received alloy exhibited a strong (13 multiple random distributions, mrd) typical basal texture where the $\{0002\}$ crystallites planes are oriented parallel to the sheet plane [45].

3.2. Microstructure and texture of the hot-rolled and annealed AZ31 alloy

Fig. 2 presents an ND-IPF map of the AZ31 alloy after hot rolling to achieve 20%, 50% and 85% thickness reduction and subsequent annealing at 350°C for 2, 10 and 60 min. The evolution of the grain size and fraction of HAGBs as a function of annealing time in the hot-rolled AZ31 samples are shown in Fig. 3. As expected, the grain size decreased with increasing thickness reduction. The grain size of 20%, 50% and 85% samples were 14.9 ± 0.4 , 6.9 ± 0.3 and $4 \pm 0.3 \mu\text{m}$, respectively. A heterogeneous microstructure could be observed in the annealed samples for 2 min, with the presence of a high fraction of LAGBs and twins, especially in the 20% and 50% hot-rolled samples. The microstructures became more homogenous with increasing annealing time, and no abnormal grain growth was evidenced. The grain size of the hot-rolled sample to 20% thickness reduction exhibits a continuous decrease with annealing time, reaching a value of $8.5 \pm 0.4 \mu\text{m}$ after 60 min. However, both 50% and 85% hot-rolled samples show a decrease in the grain size after annealing for 2 min, increasing after 10 min and then stabilising (6.3 ± 0.6 and $4.7 \pm 0.4 \mu\text{m}$ for the 50% and 85% hot-rolled samples, respectively). Notably, the microstructures of the 50% and 85% hot-rolled and annealed (for 10 min) samples shown in Fig. 2 seemed to exhibit a bimodal grain size distribution and then became more homogeneously distributed after 1 h of annealing.

Fig. 3b shows that the HAGB fraction of the deformed sample was between 25 and 35% whatever the hot-rolled thickness reduction. Annealing treatment caused an increase of the high-angle grain boundaries fraction of all samples indicating the occurrence of a recrystallisation process. The HAGB fraction after annealing for 60 min was found to be 77.3% for the 20% hot-rolled sample and 80% for the 50% and 85% hot-rolled samples.

Fig. 4 shows the variation in microhardness as a function of the annealing time of the hot-rolled AZ31 alloy at 20%, 50% and 85% thickness reduction. It should be noted that the microhardness of the as-received AZ31 alloy was equal to 72.5 ± 1.5 Hv. As expected, the 85% hot-rolled sample exhibited the highest Hv value (86.1 ± 1.2 Hv), followed by the 50% hot-rolled sample (79.5 ± 1.5 Hv) and the 20% hot-rolled sample (74 ± 1.6 Hv). The microhardness values decreased with increasing annealing time due to static recrystallisation and grain growth processes.

Figs. 5 and 6 present the GOS maps and evolution of recrystallisation fractions of the hot-rolled samples as a function of annealing time, respectively. The recrystallised grain fraction increased with increasing annealing time for all deformed samples. Furthermore, the recrystallised fraction of the 60 min annealed 20% sample was lower (87.3%) than the other annealed samples (93%). Moreover, the rate of recrystallisation increased with increasing thickness reduction. The recrystallisation fraction of the 20% hot-rolled sample was stable after annealing for 2 min and then increased with increasing annealing time. In contrast, the recrystallisation fraction after 2 min of annealing increased rapidly for the 50% and 85% hot-rolled samples. This finding might be related to stored energy increasing along with the strain level. The evolution of deformation and the recrystallisation texture is presented in Fig. 7, and the strengthening of the texture as a function of annealing time was evaluated using the following equation [46]:

$$I = \frac{1}{8\pi^2} \int_G f^2(g) \cdot dg \quad (1)$$

where I is the texture index, $f(g)$ is the ODF intensity at g orientation and G is the Euler space.

The strengthening of the basal texture decreased with increasing thickness reduction, as shown in Fig. 8. In the 20% hot-rolled sample, the basal texture remained sharp after annealing for 2 min (17 mrd) and seemed to weaken with increasing annealing time (8.1 mrd after 60 min). Consequently, the texture index of the sample continuously decreased with increasing annealing time, as shown in Fig. 8. Furthermore, the distributions of {0002} poles changed with increasing annealing time and were more distributed towards TD. Such texture

modifications during annealing treatment could be an indication of a discontinuous recrystallisation mechanism [47]. The distribution of {0002} poles towards TD developed during hot rolling to achieve 50% thickness reduction. No changes in the texture were observed with increasing annealing time, except that the texture index increased with annealing for 10 min and then decreased after 60 min of annealing. Interestingly, the texture index of both the 20% and 50% hot-rolled samples was similar after annealing for 10 and 60 min. The typical basal texture formed after 85% thickness reduction was also retained during annealing treatment. However, Fig. 8 demonstrates that the texture strengthening of the 85% hot-rolled sample increased with increasing annealing time.

3.3. Corrosion behavior of AZ31 alloy in seawater

Fig. 9a shows Nyquist plots of the as-received AZ31 alloy after hot rolling to 20%, 50% and 85% thickness reduction and subsequent annealing at 350°C for 60 min and immersion in seawater for 1 h. Notably, all samples show the presence of one capacitive loop in the high-frequency region, followed by an induction loop in the low-frequency region. The similarities in the Nyquist curves indicate that the different thermo-mechanically processed AZ31 alloy samples underwent similar corrosion mechanisms. However, differences in the evolution of capacitance diameters as a function of sample conditions indicate differences in the corrosion rate. The capacitive loop in the high-frequency region is related to the formation process of the corrosion product on the solution/metal surface, while the presence of an inductance loop in the low-frequency region is characteristic of pitting corrosion and dissolution of the protective film [48].

Fig. 9a shows that the diameter of the capacitive loop increased with increasing thickness reduction. Annealing for 60 min seemed to improve the deformed AZ31 alloy's corrosion resistance, as demonstrated by the increase in the diameter. However, the corrosion resistance of the annealed 85% hot-rolled sample was lower than that of the deformed one. To further explore the effect of deformation and annealing treatment on the corrosion mechanism of the AZ31 alloy, an electrochemical equivalent circuit was suggested, as shown in Fig. 9b. The corresponding fitting parameters of the Nyquist curves are presented in Table 2.

In the proposed equivalent circuit, R_s , R_f , R_{ct} and R_L are the solution, film, charge transfer and inductance resistance, respectively. CPE_f is a constant phase element resulting from the formation of corrosion product on the sample surface. The presence of CPE_{dl} is due to the formation of a double layer and a charge transfer reaction between the metal interface and the solution. L is an inductance parameter that expresses the occurrence and amount of

pitting corrosion [48]. Polarisation resistance can be calculated using the different resistances appearing in the equivalent circuit, as follows [49]:

$$R_p = R_s + R_f + \frac{R_{ct}R_L}{R_{ct}+R_L} \quad (2)$$

The values of R_p are presented in Table 2. The AZ31 alloy's R_p values increased along with the imposed strain, and the annealing treatment improved corrosion resistance. The R_p values increased from 109 to 223.6 $\Omega\cdot\text{cm}^2$ and from 161 to 264.13 $\Omega\cdot\text{cm}^2$ after annealing the 20% and 50% samples, respectively. Although the annealed 85% sample (96.9 $\Omega\cdot\text{cm}^2$) showed a lower value than the deformed one (174.8 $\Omega\cdot\text{cm}^2$), the corrosion resistance of the annealed 85% sample was higher than that of the as-received one (76.3 $\Omega\cdot\text{cm}^2$).

The as-received AZ31 alloy's corrosion morphology after immersion in seawater for 3 h is presented in Fig. 10 with the mean of SEM micrographs in backscatter mode at low and high resolutions. The corresponding EDS analyses (in wt.%) of 1, 2, 3 and 4 regions are also shown in Fig. 10. Notably, the morphology of the surface was not uniform, and a white-coloured compound formed and engulfed the sample surface. An EDS analysis of points 1 and 2 demonstrated the presence of high content of O (~ 52%) and Mg (~ 41%), indicating the formation of a magnesium hydroxide $\text{Mg}(\text{OH})_2$ compound rather than MgO oxide. The MgO was found to be gradually transformed into $\text{Mg}(\text{OH})_2$ with increasing immersion time [38]. Moreover, the thickness of MgO was found to decrease with increasing Al content in Mg-Al alloys [50]. A relatively high amount of Cl (~ 3%) was also observed in these areas. The corrosion morphology also showed the presence of cracks (as shown by arrows), mainly due to the dehydration of the corrosion product. The high resolution of the region delimited by the yellow square shows the presence of small 'mushrooms-like' morphology. Similar morphologies were reported in an Mg-RE alloy corroded in a 3.5% NaCl solution [51]. The EDS analysis of points 3 and 4 indicates the presence of O and Mg. Interestingly, the amount of Cl in these points was lower than for points 1 and 2. The high resolution of the red-square region shows the typical corrosion morphology of needle-like particles frequently reported in Mg-based alloys [51, 52].

4. Discussion

The present study aimed to investigate the effect of hot-rolling at low, medium and high strain (i.e., 20%, 50% and 85% thickness reduction, respectively) on the evolution of the microstructure, texture and corrosion behavior in AZ31 alloy during isothermal annealing.

4.1. Deformation microstructure and texture

As shown in Figs. 2 and 3, grain size decreased with increasing strain. However, the HAGBs first decreased with increasing strain at 50% thickness reduction (24.6%) and then increased at 85% thickness reduction (31.8%), mainly due to the occurrence of DRX. Fig. 5 and the evolution of recrystallised fraction, as shown in Fig. 6, demonstrate that the AZ31 alloy underwent DRX during hot working only at medium and high strain (i.e., 50% and 85% thickness reduction). The absence of DRX in the 20% hot-rolled sample may be explained by the deformation strain level being insufficient to cause DRX. The microstructure looks similar to the as-received AZ31 alloy, as shown in Fig. 1a.

The kernel average misorientation (KAM) approach is commonly used to estimate the distribution of strain and dislocation density in individual measured points [53]. Generally, the KAM method allows quantifying the average misorientation between a given point and its nearest neighbours belonging to the same grain. Fig. 11 presents the KAM maps and corresponding distributions in the hot-rolled AZ31 alloy for the three thickness reductions. The KAM was calculated using third-neighbor distance and 5° as the maximum misorientation angle. Several grains in the 20% hot-rolled sample were blue in colour with an assigned misorientation of less than 1° and were considered un-deformed regions. The strain mainly accumulated near the grain boundaries and specifically LAGBs (green colour). The KAM level increased ($KAM_{avg} = 2.13^\circ$) after 50% thickness reduction due to the deformation process and increased dislocation density. Despite increasing the thickness reduction up to 85%, the mean KAM value seemed to remain stable ($KAM_{avg} = 2.11^\circ$). Additionally, the 85% hot-rolled sample contains some blue-coloured grains (low KAM value), mainly due to the occurrence of DRX, as shown in GOS map (Fig. 5).

However, microhardness values increased (Fig. 4) between 50% and 85% thickness reduction, indicating a continuous increase in dislocation density. Dislocations that accumulate in the deformed microstructure are commonly categorised into geometrically necessary dislocations (GNDs) and statistically stored dislocations (SSDs). The KAM approach can only estimate the density of GNDs [54], while microhardness measurements allow both types to be estimated [55]. It has been reported that GNDs are responsible for the increase in stored energy in the initial stage of deformation, and their contribution subsequently decreases due to the occurrence of DRX. However, the contribution of SSDs increases along with increasing strain to ensure deformation accommodation [56].

Increasing strain generates new orientations, as shown in the ND-IPF map (Fig. 2) and the evolution of deformation texture (Fig. 7). At low strain (20% thickness reduction), the

typical basal texture was observed, as the $\{0002\}$ poles were parallel to the sheet plane. The high recorded intensity (~ 18 mrd) was mainly due to poor grain statistics, as shown in the ND-IPF map. Otherwise, for the other hot-rolled samples, texture intensity should increase along with increasing thickness reduction. Texture sharpening upon increasing thickness reduction is often reported in rolled Mg-based alloys [57-59]. Texture development is usually strongly related to the deformation mechanisms [60]. At medium strain (50% thickness reduction), the $\{0002\}$ basal poles are more distributed towards TD. The change in the texture may be related to the presence of mechanical twinning [19].

It is known that the formation of twins during deformation strongly affects the resulting texture by changing the orientation of the lattice structure [61, 62]. Close inspection of the ND-IPF maps (Fig. 2) clearly indicates that the twins are more frequently evidenced in the 50% hot-rolled sample than in other samples. The fractions of common twin modes (i.e., $\{10\bar{1}2\}$ extension twin, $\{10\bar{1}1\}$ contraction twin and $\{10\bar{1}1\}$ - $\{10\bar{1}2\}$ or $\{10\bar{1}3\}$ - $\{10\bar{1}2\}$ double twins) in the hot-rolled samples are listed in Table 3. Unexpectedly, the 20% hot-rolled sample presented a very low fraction of twins, especially $\{10\bar{1}2\}$ extension twins. The presence of twins was evidenced by optical microscope in the AZ31 alloy under similar conditions (hot-rolling to achieve 20% thickness reduction) [38]. Further, optical microscope observations demonstrated the formation of twins only after 5% thickness reduction in an AZ31 alloy sample hot-rolled at 300°C [36]. The absence of twins at low strain in the presently studied alloy might be related to the as-received microstructure. Indeed, the as-received AZ31 alloy exhibited a deformation microstructure. Twin generation was retarded by pre-existing dislocations in the as-received alloy, which might increase the energy barriers for twin nucleation [63]. The number of twins increased along with strain, as shown in the 50% hot-rolled sample. All twin modes were present, except contraction twins (1.3%). A higher fraction of double $22^\circ \langle 11\bar{2}0 \rangle$ twins was observed in the 85% hot-rolled sample. The decrease in twin fractions in the 85% hot-rolled sample could be correlated with the decrease in grain size [59, 64]. The generation of twins is hindered with decreasing grain size because the distribution of stress in fine grains is unfavourable for twin activation, while in coarse grains, it is considerably more advantageous [59].

Fig. 12 presents a selected region of the ND-IPF map (Fig. 2) of the 50% hot-rolled sample containing different twin modes. Different twin morphologies were observed in the hot-rolled sample. The misorientation profile along segments A to B indicate a step-like morphology, which form from double twins. A similar twin structure has been reported in several Mg-based alloys [27, 60]. The development of this twin step is governed by

homogeneity in the stress distribution and strain level [27]. The misorientation profile along segments C to D show different types of twins. The corresponding {0002} pole figure indicates that different mechanical twinings were able to change or create different orientations from the typical basal texture. The extension twin caused a rotation of about 86° in the {0002} plane, leading to the formation of {0002}//RD. In contrast, both contraction and double twins caused a deviation of {0002} basal poles towards TD.

In the literature, it has been reported that weakening of the basal texture is caused by the activation of twins and non-basal slip systems (i.e., $\langle a \rangle$ prismatic and $\langle c+a \rangle$ pyramidal slip) [65]. Indeed, the activation of prismatic $\langle a \rangle$ slip contributed to the deviation of basal poles about $20\text{--}40^\circ$ from ND towards TD [66]. This corroborates the texture of the 50% hot-rolled sample. However, a typical basal texture developed with increasing strain in the 85% hot-rolled sample. The decrease in the twin fraction and activation of a $\langle c+a \rangle$ pyramidal slip in the deformed sample could explain the disappearance of deviation towards TD. It has been demonstrated by visco-plastic self-consistent (VPSC) simulation that the activation of a $\langle c+a \rangle$ pyramidal slip causes the splitting of the basal pole towards RD [57]. Moreover, it was expected that the $\langle c+a \rangle$ pyramidal slip would be more activated in the hot-rolled 85% sample since it is assumed that its activation increases along with thickness reduction [58].

The variation in texture as a function of thickness reduction is also commonly related to the occurrence of DRX. As shown in Figs. 5 and 6, the fraction of dynamic recrystallised grains increased along with thickness reduction. The textures of deformed and recrystallised grains of the AZ31 alloy hot-rolled to 50% and 85% thickness reduction are separately presented in Fig. 13 by means of recalculated {0002} pole figures. The orientations of recrystallised grains in the 50% hot-rolled sample differed from the deformed ones. The formation of an {0002}//RD orientation is an indication of a twin-induced DRX mechanism [16]. In fact, the twins contain high levels of stored energy and can act as favourable sites for DRX. Some reports demonstrated that such mechanism resulted in similar orientations than the host twin [35, 36]. However, the orientations of recrystallised and deformed grains were similar for the 85% hot-rolled sample. The difference in the orientation of dynamically recrystallised grains of the two hot-rolled samples suggest different nucleation behaviours during DRX. The change in 50% hot-rolled sample recrystallised grain orientations could be related to its high deformation microstructure heterogeneity, which made a wide variety of orientations available for recrystallisation nucleation. In the 85% hot-rolled sample, the orientation of dynamically recrystallised grains seems to be limited to the basal orientation {0002}//ND initially present in the deformed microstructure.

4.2. Recrystallisation microstructure and texture

The annealing treatment at 350°C for 2–60 min resulted in normal grain growth for all hot-rolled samples, as shown in Figs. 2 and 3. The small variation in grain-size values as a function of annealing time (Fig. 3a) indicate appreciable grain refinement when compared to the as-received state. However, the evolution of HAGBs as a function of annealing time (Fig. 3b) shows that even after annealing for 60 min, the microstructure contained LAGBs (25%, 20% and 18% for 20%, 50% and 85% hot-rolled samples, respectively) and may indicate that recrystallisation was incomplete. The presence of LAGBs was attributed to the basal texture, which resulted in low grain boundary misorientation between grains with similar orientations.

The evolution of recrystallised fractions as a function of annealing time indicates that the 20% hot-rolled sample needed a 2-min incubation time (Fig. 6). The incubation time decreased with increasing thickness reduction. Increasing deformation defects also increased the nucleation sites for recrystallisation, thereby increasing the recrystallisation rate. Moreover, a close analysis of the GOS maps of hot-rolled samples suggests that the DRX fraction increased with increasing thickness reduction. These dynamically recrystallised grains worked as a ‘precursor’ that reduced the incubation time for static recrystallisation during annealing. Grain size was much smaller in the 85% hot-rolled sample compared to the other hot-rolled samples, which is consistent with the statement that increasing the recrystallisation rate prevents grain coarsening [25].

Furthermore, annealing the low-strained sample (20% thickness reduction) caused the spreading of basal poles from ND towards TD, while no changes in the recrystallisation texture were observed in the medium- and high-strained samples (Fig. 7). Fig. 14 presents the evolution of the recalculated {0002} pole figure for deformed and recrystallised grains as a function of the annealing time of the hot-rolled AZ31 alloy after 20%, 50% and 85% thickness reduction. The texture of recrystallised grains in the 20% hot-rolled sample differs from the deformed one, while the textures of the recrystallised grains in 50% and 85% hot-rolled samples are very similar to the deformed one. The particular {0002}// RD orientation found in the DRX grains of the 50% hot-rolled sample (Fig. 13) disappeared upon annealing. It has been suggested that grains with a {0002} basal orientation are prone to higher nucleation rates when compared to other orientations, which makes them more likely to vanish; thus, the {0002} basal orientation dominates the recrystallisation texture [24]. Consequently, the occurrence of DRX in the 50% and 85% hot-rolled samples prevented texture changes during static recrystallisation. Furthermore, the increased texture index of

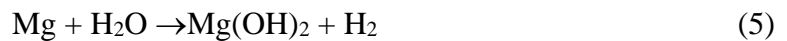
both 50% and 85% rolled samples during annealing treatment indicates that DRX caused net recrystallisation texture sharpening, especially in the 85% hot-rolled sample.

In the literature, several phenomena have been associated with variation in the recrystallisation texture, including deformation heterogeneities [67], particle-stimulated nucleation of recrystallisation (PSN) [68], solute drag [69] and abnormal grain growth [70]. PSN and abnormal grain growth could not have been responsible for the texture change in the present alloy since neither was clearly evidenced by EBSD analysis. However, the effect of solute (Al and Zn) elements on grain boundary mobility can be excluded since only one AZ31 alloy (with fixed composition) was used in the present study.

DRX could be responsible for texture changes in the hot-rolled sample at low strain (20% thickness reduction). At low strain, the sample did not undergo DRX, unlike the samples hot rolled at medium and high strain. The low deformation strain could be insufficient to begin DRX. It was observed that recrystallisation texture weakening in the hot-rolled AZ31 alloy was more effective when no DRX occurred [25]. The incubation time of 2 min indicates that the 20% hot-rolled sample could recover before the recrystallisation process. The recovery process caused the annihilation of SSDs, which allowed GNDs to transform into cell boundaries, leading to the formation of sub-grains with widespread basal pole orientations. In addition, the low strain level may increase the likelihood of a wide range of orientations to nucleate and, therefore, result in dispersion of the texture (see Fig. 2).

4.3. Effect of microstructure and texture variation on corrosion behavior

Corrosion morphology and EDS analyses of the corroded surface of the as-received AZ31 alloy (Fig. 10) revealed the formation of $\text{Mg}(\text{OH})_2$, a typical corrosion product formed when the Mg-based alloys are immersed in an aqueous solution. The formation of $\text{Mg}(\text{OH})_2$ compounds is often accompanied by hydrogen evolution based on the following equations [71]:



The Nyquist plots and fitted parameters shown in Fig. 9 and Table 3 demonstrate that the AZ31 alloy's corrosion resistance increased along with thickness reduction. Based on the evolution of the deformation microstructure, it can be concluded that improved corrosion

resistance is due to decreased grain size and the occurrence of DRX, especially in the 85% hot-rolled sample. Several reports have demonstrated that grain refinement improves the corrosion resistance of many processed Mg-based alloys [20, 72-74]. Decreasing grain size means increasing the fraction of grain boundaries, which ensures uniform corrosion product distribution across the sample surface and, consequently, decreased dissolution of the Mg matrix. It was demonstrated recently that galvanic corrosion preferentially occurs in the deformed region rather than dynamically the recrystallised region [75]. This finding is consistent with the present results, where the 85% hot-rolled sample shows the highest fraction of DRX.

However, it has previously been reported that the corrosion resistance of an as-received AZ31 sample was better than those hot-rolled to 20% and 50% thickness in 0.9% NaCl solution [38]. Moreover, severe plastic deformation processing via high pressure torsion (HPT) of AZ31 and ZK60 alloys showed no significant effect on corrosion behavior when testing in a 3.5% NaCl solution [76]. The difference in corrosion behavior in the present study could be attributed to the nature of the immersion solution. It is expected that an artificial NaCl solution would be more aggressive than seawater. On average, seawater has a salinity of approximately 3.5% and a relative ion concentration as follows: magnesium 0.129%, chlorine 1.95%, potash 0.038%, bromine 0.067%, sodium 1.077% and calcium 0.0412% [77]. In addition to the presence of these different elements, seawater contains pollutants and decomposed organic matter, which affect the corrosion behavior of the alloy. The corrosion rate of austenitic stainless steel was found to be lower in seawater than in artificial 3.5% NaCl solution [78]. Recently, it was evidenced that alloys with small grain sizes corrode more easily in aggressive corrosion media [79].

Fig. 9 and Table 3 show that annealing treatment for 60 min at 350°C also led to increased corrosion resistance of all hot-rolled samples except for the 85% hot-rolled sample. The results reveal that the annealed 50% hot-rolled sample showed excellent corrosion resistance. This could be associated with an optimal combination of grain refinement and texture weakening. It has been reported that grains of an AZ31 alloy with a {0002} basal orientation are less corroded in 3.5% NaCl solution than grains with a {10 $\bar{1}$ 0} prismatic orientation [80]. The present study indicates that the {0002} basal pole's deviation towards TD could be responsible for improved corrosion resistance when compared to the typical basal texture observed in the annealed 85% hot-rolled sample. In future research, it would be interesting to further investigate the effect of {0002} basal pole deviation and its ideal position on the corrosion behavior of an AZ31 alloy.

5. Conclusions

The microstructure and texture of an AZ31 alloy were investigated after hot rolling at 350°C to 20%, 50% and 85% thickness reduction and subsequent annealing at 350°C for 2–60 min. Furthermore, the effect of hot rolling and static recrystallisation on the AZ31 alloy's corrosion behavior in seawater was evaluated.

- A low fraction of twins was observed at low strain (20% thickness reduction), likely due to the deformation state of the as-received alloy. A high fraction of $\{10\bar{1}2\}$ extension twins was observed at medium strain (50% thickness reduction). However, the microstructure of the high strain (85% thickness reduction) sample was characterised by the occurrence of DRX.
- The presence of twins and DRX strongly affected the deformation texture.
- Annealing at 350°C for up to 60 min led to normal grain growth in all hot-rolled samples. The deformation texture was retained in annealed 50% and 85% hot-rolled samples, while a net change in the recrystallisation texture was observed after 2 min of annealing in the 20% hot-rolled sample. This behavior was attributed to the absence of DRX in the latter sample.
- A combination of grain refinement and texture weakening was responsible for improving the of AZ31 alloy's corrosion resistance in seawater.

Acknowledgments

The authors are grateful to Dr Ing. Norbert Hort and Dr DietmarLetzig of the Magnesium Innovations Center (MagIC) in Germany for kindly providing the AZ31 alloy. The authors would also like to thank Dr Kamel Tirsatine for his help with the rolling process. This work was supported by the PRFU national project under grant agreement no. B00L02UN280120180005.

Funding: “This research was funded by PRFU national project under Grant Agreement No. B00L02UN280120180005”.

Conflicts of Interest: The authors declare no conflict of interest.

Data Availability: The raw/processed data required to reproduce these findings cannot be shared at this time as the data also forms part of an ongoing study.

References

- [1] K.U. Kainer, Challenges for Implementation of Magnesium into More Applications, in: A. Singh, K. Solanki, M.V. Manuel, N.R. Neelameggham (Eds.) *Magnesium Technology 2016*, Springer International Publishing, Cham, 2016, pp. 5-6.
- [2] A. Luo, Applications: Aerospace, automotive and other structural applications of magnesium, *Fundamentals of Magnesium Alloy Metallurgy*, (2013) 266-316. DOI: 10.1533/9780857097293.266.
- [3] S. Kleinbaum, in: V.V. Joshi, J.B. Jordon, D. Orlov, N.R. Neelameggham (Eds.) *Magnesium Technology 2019*, Springer International Publishing, Cham, 2019, pp. 13-14.
- [4] B.L. Mordike, T. Ebert, Magnesium: Properties — applications — potential, *Materials Science and Engineering: A*, 302 (2001) 37-45. DOI: [https://doi.org/10.1016/S0921-5093\(00\)01351-4](https://doi.org/10.1016/S0921-5093(00)01351-4).
- [5] H. Azzeddine, D. Bradai, On the texture and grain growth in hot-deformed and annealed WE54 alloy, *International Journal of Materials Research*, 103 (2012) 1351-1360. DOI: 10.3139/146.110768.
- [6] A. Atrens, G.-L. Song, M. Liu, Z. Shi, F. Cao, M.S. Dargusch, Review of Recent Developments in the Field of Magnesium Corrosion, *Advanced Engineering Materials*, 17 (2015) 400-453. DOI: 10.1002/adem.201400434.
- [7] M.R. Barnett, Influence of deformation conditions and texture on the high temperature flow stress of magnesium AZ31, *Journal of Light Metals*, 1 (2001) 167-177. DOI: [https://doi.org/10.1016/S1471-5317\(01\)00010-4](https://doi.org/10.1016/S1471-5317(01)00010-4).
- [8] K. Matsubara, Y. Miyahara, Z. Horita, T.G. Langdon, Developing superplasticity in a magnesium alloy through a combination of extrusion and ECAP, *Acta Materialia*, 51 (2003) 3073-3084. DOI: [https://doi.org/10.1016/S1359-6454\(03\)00118-6](https://doi.org/10.1016/S1359-6454(03)00118-6).
- [9] T. Al-Samman, G. Gottstein, Dynamic recrystallization during high temperature deformation of magnesium, *Materials Science and Engineering: A*, 490 (2008) 411-420. DOI: <https://doi.org/10.1016/j.msea.2008.02.004>.
- [10] S. Sandlöbes, I. Schestakow, S.B. Yi, S. Zaeferrer, J.Q. Chen, M. Friák, J. Neugebauer, D. Raabe, The Relation between Shear Banding, Microstructure and Mechanical Properties in Mg and Mg-Y Alloys, *Materials Science Forum*, 690 (2011) 202-205. DOI: 10.4028/www.scientific.net/MSF.690.202.
- [11] H. Azzeddine, D. Bradai, On some aspects of compressive properties and serrated flow in Mg-Y-Nd-Zr alloy, *Journal of Rare Earths*, 31 (2013) 804-810. DOI: [https://doi.org/10.1016/S1002-0721\(12\)60362-7](https://doi.org/10.1016/S1002-0721(12)60362-7).

- [12] D. Elfiad, Y.I. Bourezg, H. Azzeddine, D. Bradai, Investigation of texture, microstructure, and mechanical properties of a magnesium–lanthanum alloy after thermo-mechanical processing, *International Journal of Materials Research*, 107 (2016) 315-323. DOI: 10.3139/146.111347.
- [13] A. Hanna, H. Azzeddine, R. Lachhab, T. Baudin, A.-L. Helbert, F. Brisset, Y. Huang, D. Bradai, T.G. Langdon, Evaluating the textural and mechanical properties of an Mg-Dy alloy processed by high-pressure torsion, *Journal of Alloys and Compounds*, 778 (2019) 61-71. DOI: <https://doi.org/10.1016/j.jallcom.2018.11.109>.
- [14] M. Kaviani, G.R. Ebrahimi, H.R. Ezatpour, Improving the mechanical properties and biocorrosion resistance of extruded Mg-Zn-Ca-Mn alloy through hot deformation, *Materials Chemistry and Physics*, 234 (2019) 245-258. DOI: <https://doi.org/10.1016/j.matchemphys.2019.06.010>.
- [15] S.M. Fatemi, H. Paul, Characterization of continuous dynamic recrystallization in WE43 magnesium alloy, *Materials Chemistry and Physics*, 257 (2021) 123726. DOI: <https://doi.org/10.1016/j.matchemphys.2020.123726>.
- [16] O. Sitdikov, R. Kaibyshev, T. Sakai, Dynamic Recrystallization Based on Twinning in Coarse-Grained Mg, *Materials Science Forum*, 419-422 (2003) 521-526. DOI: 10.4028/www.scientific.net/MSF.419-422.521.
- [17] S.E. Ion, F.J. Humphreys, S.H. White, Dynamic recrystallisation and the development of microstructure during the high temperature deformation of magnesium, *Acta Metallurgica*, 30 (1982) 1909-1919. DOI: [https://doi.org/10.1016/0001-6160\(82\)90031-1](https://doi.org/10.1016/0001-6160(82)90031-1).
- [18] F.J. Humphreys, M. Hatherly, Chapter 7 - Recrystallization of Single-Phase Alloys, in: F.J. Humphreys, M. Hatherly (Eds.) *Recrystallization and Related Annealing Phenomena* (Second Edition), Elsevier, Oxford, 2004, pp. 215-IV.
- [19] M.R. Barnett, M.D. Nave, C.J. Bettles, Deformation microstructures and textures of some cold rolled Mg alloys, *Materials Science and Engineering: A*, 386 (2004) 205-211. DOI: <https://doi.org/10.1016/j.msea.2004.07.030>.
- [20] T. Abu Leil, N. Hort, W. Dietzel, C. Blawert, Y. Huang, K.U. Kainer, K.P. Rao, Microstructure and corrosion behavior of Mg-Sn-Ca alloys after extrusion, *Transactions of Nonferrous Metals Society of China*, 19 (2009) 40-44. DOI: [https://doi.org/10.1016/S1003-6326\(08\)60225-3](https://doi.org/10.1016/S1003-6326(08)60225-3).
- [21] S. Abdessameud, H. Azzeddine, B. Alili, D. Bradai, Grain growth in AZ31 alloy after uniaxial compression, *Transactions of Nonferrous Metals Society of China*, 20 (2010) 2215-2222. DOI: [https://doi.org/10.1016/S1003-6326\(10\)60631-0](https://doi.org/10.1016/S1003-6326(10)60631-0).

- [22] T. Al-Samman, Modification of texture and microstructure of magnesium alloy extrusions by particle-stimulated recrystallization, *Materials Science and Engineering: A*, 560 (2013) 561-566. DOI: <https://doi.org/10.1016/j.msea.2012.09.102>.
- [23] J.J. Bhattacharyya, S.R. Agnew, G. Muralidharan, Texture enhancement during grain growth of magnesium alloy AZ31B, *Acta Materialia*, 86 (2015) 80-94. DOI: <https://doi.org/10.1016/j.actamat.2014.12.009>.
- [24] Y. Wang, Y. Xin, Q. Liu, Annealing induced concentration of basal poles toward the normal direction of a hot rolled Mg–5.7Zn plate, *Journal of Alloys and Compounds*, 666 (2016) 341-345. DOI: <https://doi.org/10.1016/j.jallcom.2015.12.253>.
- [25] J. Su, S. Yue, in: K.N. Solanki, D. Orlov, A. Singh, N.R. Neelameggham (Eds.) *Magnesium Technology 2017*, Springer International Publishing, Cham, 2017, pp. 547-554.
- [26] D. Guan, W.M. Rainforth, L. Ma, B. Wynne, J. Gao, Twin recrystallization mechanisms and exceptional contribution to texture evolution during annealing in a magnesium alloy, *Acta Materialia*, 126 (2017) 132-144. DOI: <https://doi.org/10.1016/j.actamat.2016.12.058>.
- [27] J.-x. Liu, K. Liu, W.-b. Du, S.-b. Li, Z.-h. Wang, X. Du, C.-c. Sun, Effect of temperature on microstructure and texture evolution of Mg-Zn-Er alloy during hot compression, *Transactions of Nonferrous Metals Society of China*, 28 (2018) 2214-2225. DOI: [https://doi.org/10.1016/S1003-6326\(18\)64866-6](https://doi.org/10.1016/S1003-6326(18)64866-6).
- [28] A. Imandoust, C.D. Barrett, T. Al-Samman, M.A. Tschopp, E. Essadiqi, N. Hort, H. El Kadiri, Unraveling Recrystallization Mechanisms Governing Texture Development from Rare-Earth Element Additions to Magnesium, *Metallurgical and Materials Transactions A*, 49 (2018) 1809-1829. DOI: [10.1007/s11661-018-4520-8](https://doi.org/10.1007/s11661-018-4520-8).
- [29] X. Zeng, P. Minárik, P. Dobroň, D. Letzig, K.U. Kainer, S. Yi, Role of deformation mechanisms and grain growth in microstructure evolution during recrystallization of Mg-Nd based alloys, *Scripta Materialia*, 166 (2019) 53-57. DOI: <https://doi.org/10.1016/j.scriptamat.2019.02.045>.
- [30] S.S.A. Shah, D. Wu, R.S. Chen, G.S. Song, Static recrystallization behavior of multi-directional impact forged Mg-Gd-Y-Zr alloy, *Journal of Alloys and Compounds*, 805 (2019) 189-197. DOI: <https://doi.org/10.1016/j.jallcom.2019.07.086>.
- [31] A. Hanna, H. Azzeddine, Y. Huang, D. Bradai, J.M. Cabrera, T.G. Langdon, An investigation of the thermal stability of an MgDy alloy after processing by high-pressure torsion, *Materials Characterization*, 151 (2019) 519-529. DOI: <https://doi.org/10.1016/j.matchar.2019.03.040>.

- [32] Q. Wang, B. Jiang, A. Tang, J. Fu, Z. Jiang, H. Sheng, D. Zhang, G. Huang, F. Pan, Unveiling annealing texture formation and static recrystallization kinetics of hot-rolled Mg-Al-Zn-Mn-Ca alloy, *Journal of Materials Science & Technology*, 43 (2020) 104-118. DOI: <https://doi.org/10.1016/j.jmst.2020.01.018>.
- [33] K.D. Molodov, T. Al-Samman, D.A. Molodov, G. Gottstein, Mechanisms of exceptional ductility of magnesium single crystal during deformation at room temperature: Multiple twinning and dynamic recrystallization, *Acta Materialia*, 76 (2014) 314-330. DOI: <https://doi.org/10.1016/j.actamat.2014.04.066>.
- [34] J.H. Kim, B.-C. Suh, T.T.T. Trang, J.H. Hwang, N.J. Kim, Orientations of dynamically recrystallized grains nucleated at double twins in Mg-4Zn-1Sn alloy, *Scripta Materialia*, 170 (2019) 11-15. DOI: <https://doi.org/10.1016/j.scriptamat.2019.05.029>.
- [35] T. Al-Samman, K.D. Molodov, D.A. Molodov, G. Gottstein, S. Suwas, Softening and dynamic recrystallization in magnesium single crystals during c-axis compression, *Acta Materialia*, 60 (2012) 537-545. DOI: <https://doi.org/10.1016/j.actamat.2011.10.013>.
- [36] M. Wang, R. Xin, B. Wang, Q. Liu, Effect of initial texture on dynamic recrystallization of AZ31 Mg alloy during hot rolling, *Materials Science and Engineering: A*, 528 (2011) 2941-2951. DOI: <https://doi.org/10.1016/j.msea.2010.11.069>.
- [37] S. Abdessameud, D. Bradai, Microstructure and Texture Evolution in Hot Rolled and Annealed Magnesium Alloy TRC AZ31, *Canadian Metallurgical Quarterly*, 48 (2009) 433-442. DOI: 10.1179/cmq.2009.48.4.433.
- [38] A. Hanna, A. Dakhouche, K. Tirsatine, A. Sari, Y. Khereddine, D. Bradai, H. Azzeddine, Effect of hot rolling on the corrosion behavior of AZ31 magnesium alloy, *Metall. Res. Technol.*, 116 (2019) 109.
- [39] Y. Mikami, K. Oda, M. Kamaya, M. Mochizuki, Effect of reference point selection on microscopic stress measurement using EBSD, *Materials Science and Engineering: A*, 647 (2015) 256-264. DOI: <https://doi.org/10.1016/j.msea.2015.09.004>.
- [40] R. Hielscher, H. Schaeben, A novel pole figure inversion method: specification of the MTEX algorithm, *Journal of Applied Crystallography*, 41 (2008) 1024-1037. DOI: 10.1107/s0021889808030112.
- [41] J.-H. Cho, A.D. Rollett, K.H. Oh, Determination of a mean orientation in electron backscatter diffraction measurements, *Metallurgical and Materials Transactions A*, 36 (2005) 3427-3438. DOI: 10.1007/s11661-005-0016-4.

- [42] C. Drouven, I. Basu, T. Al-Samman, S. Korte-Kerzel, Twinning effects in deformed and annealed magnesium–neodymium alloys, *Materials Science and Engineering: A*, 647 (2015) 91-104. DOI: <https://doi.org/10.1016/j.msea.2015.08.090>.
- [43] C.D. Barrett, A. Imandoust, A.L. Oppedal, K. Inal, M.A. Tschopp, H. El Kadiri, Effect of grain boundaries on texture formation during dynamic recrystallization of magnesium alloys, *Acta Materialia*, 128 (2017) 270-283. DOI: <https://doi.org/10.1016/j.actamat.2017.01.063>.
- [44] S. Tighiouaret, R. Lachhab, A. Hanna, H. Azzeddine, Y. Huang, T. Baudin, A.-L. Helbert, F. Brisset, D. Bradai, T.G. Langdon, Thermal Stability of an Mg–Nd Alloy Processed by High-Pressure Torsion, *Advanced Engineering Materials*, 21 (2019) 1900801. DOI: [10.1002/adem.201900801](https://doi.org/10.1002/adem.201900801).
- [45] H. Watanabe, T. Mukai, K. Ishikawa, Effect of temperature of differential speed rolling on room temperature mechanical properties and texture in an AZ31 magnesium alloy, *Journal of Materials Processing Technology*, 182 (2007) 644-647. DOI: <https://doi.org/10.1016/j.jmatprotec.2006.08.010>.
- [46] H.-J. Bunge, *Texture Analysis in Materials Science*, 1st edition ed., Butterworth-Heinemann, 1982.
- [47] J. Victoria-Hernandez, S. Yi, J. Bohlen, G. Kurz, D. Letzig, The influence of the recrystallization mechanisms and grain growth on the texture of a hot rolled AZ31 sheet during subsequent isochronal annealing, *Journal of Alloys and Compounds*, 616 (2014) 189-197. DOI: <https://doi.org/10.1016/j.jallcom.2014.07.083>.
- [48] Z. Shi, F. Cao, G.-L. Song, M. Liu, A. Atrens, Corrosion behaviour in salt spray and in 3.5% NaCl solution saturated with Mg(OH)₂ of as-cast and solution heat-treated binary Mg–RE alloys: RE=Ce, La, Nd, Y, Gd, *Corrosion Science*, 76 (2013) 98-118. DOI: <https://doi.org/10.1016/j.corsci.2013.06.032>.
- [49] T. Zhang, Y. Shao, G. Meng, Z. Cui, F. Wang, Corrosion of hot extrusion AZ91 magnesium alloy: I-relation between the microstructure and corrosion behavior, *Corrosion Science*, 53 (2011) 1960-1968. DOI: <https://doi.org/10.1016/j.corsci.2011.02.015>.
- [50] D. Daloz, P. Steinmetz, G. Michot, Corrosion Behavior of Rapidly Solidified Magnesium-Aluminum-Zinc Alloys, *Corrosion*, 53 (1997) 944-954. DOI: [10.5006/1.3290279](https://doi.org/10.5006/1.3290279).
- [51] H. Azzeddine, A. Hanna, A. Dakhouche, L. Rabahi, N. Scharnagl, M. Dopita, F. Brisset, A.-L. Helbert, T. Baudin, Impact of rare-earth elements on the corrosion performance of binary magnesium alloys, *Journal of Alloys and Compounds*, 829 (2020) 154569. DOI: <https://doi.org/10.1016/j.jallcom.2020.154569>.

- [52] Y. Song, E.-H. Han, K. Dong, D. Shan, C.D. Yim, B.S. You, Study of the corrosion product films formed on the surface of Mg-xZn alloys in NaCl solution, *Corrosion Science*, 88 (2014) 215-225. DOI: <https://doi.org/10.1016/j.corsci.2014.07.034>.
- [53] Y. Ateba Betanda, A.-L. Helbert, F. Brisset, M.-H. Mathon, T. Waeckerlé, T. Baudin, Measurement of stored energy in Fe-48%Ni alloys strongly cold-rolled using three approaches: Neutron diffraction, Dillamore and KAM approaches, *Materials Science and Engineering: A*, 614 (2014) 193-198. DOI: <https://doi.org/10.1016/j.msea.2014.07.037>.
- [54] W. Pantleon, Resolving the geometrically necessary dislocation content by conventional electron backscattering diffraction, *Scripta Materialia*, 58 (2008) 994-997. DOI: <https://doi.org/10.1016/j.scriptamat.2008.01.050>.
- [55] S.S. Hazra, A.A. Gazder, E.V. Pereloma, Stored energy of a severely deformed interstitial free steel, *Materials Science and Engineering: A*, 524 (2009) 158-167. DOI: <https://doi.org/10.1016/j.msea.2009.06.033>.
- [56] H. Azzeddine, K. Tirsatine, T. Baudin, M.-H. Mathon, A.-L. Helbert, F. Brisset, D. Bradai, On the stored energy evolution after accumulative roll-bonding of invar alloy, *Materials Chemistry and Physics*, 201 (2017) 408-415. DOI: <https://doi.org/10.1016/j.matchemphys.2017.08.063>.
- [57] S.R. Agnew, M.H. Yoo, C.N. Tomé, Application of texture simulation to understanding mechanical behavior of Mg and solid solution alloys containing Li or Y, *Acta Materialia*, 49 (2001) 4277-4289. DOI: [https://doi.org/10.1016/S1359-6454\(01\)00297-X](https://doi.org/10.1016/S1359-6454(01)00297-X).
- [58] M.T. Pérez-Prado, J.A. del Valle, J.M. Contreras, O.A. Ruano, Microstructural evolution during large strain hot rolling of an AM60 Mg alloy, *Scripta Materialia*, 50 (2004) 661-665. DOI: <https://doi.org/10.1016/j.scriptamat.2003.11.014>.
- [59] D. Liu, Z.-y. Liu, E.-d. Wang, Evolution of twins and texture and its effects on mechanical properties of AZ31 magnesium alloy sheets under different rolling process parameters, *Transactions of Nonferrous Metals Society of China*, 25 (2015) 3585-3594. DOI: [https://doi.org/10.1016/S1003-6326\(15\)63999-1](https://doi.org/10.1016/S1003-6326(15)63999-1).
- [60] L.W.F. Mackenzie, M. Pekguleryuz, The influences of alloying additions and processing parameters on the rolling microstructures and textures of magnesium alloys, *Materials Science and Engineering: A*, 480 (2008) 189-197. DOI: <https://doi.org/10.1016/j.msea.2007.07.003>.
- [61] X.-y. Yang, Z.-s. Ji, H. Miura, T. Sakai, Dynamic recrystallization and texture development during hot deformation of magnesium alloy AZ31, *Transactions of Nonferrous*

Metals Society of China, 19 (2009) 55-60. DOI: [https://doi.org/10.1016/S1003-6326\(08\)60228-9](https://doi.org/10.1016/S1003-6326(08)60228-9).

[62] Y. Pei, A. Godfrey, J. Jiang, Y.B. Zhang, W. Liu, Q. Liu, Extension twin variant selection during uniaxial compression of a magnesium alloy, *Materials Science and Engineering: A*, 550 (2012) 138-145. DOI: <https://doi.org/10.1016/j.msea.2012.04.046>.

[63] P. Chen, B. Li, D. Culbertson, Y. Jiang, in: D. Orlov, V. Joshi, K.N. Solanki, N.R. Neelameggham (Eds.) *Magnesium Technology 2018*, Springer International Publishing, Cham, 2018, pp. 193-198.

[64] Y. Chino, K. Kimura, M. Hakamada, M. Mabuchi, Mechanical anisotropy due to twinning in an extruded AZ31 Mg alloy, *Materials Science and Engineering: A*, 485 (2008) 311-317. DOI: <https://doi.org/10.1016/j.msea.2007.07.076>.

[65] L.-l. Guo, F. Fujita, Effect of deformation mode, dynamic recrystallization and twinning on rolling texture evolution of AZ31 magnesium alloys, *Transactions of Nonferrous Metals Society of China*, 28 (2018) 1094-1102. DOI: [https://doi.org/10.1016/S1003-6326\(18\)64745-4](https://doi.org/10.1016/S1003-6326(18)64745-4).

[66] Y.N. Wang, J.C. Huang, Texture analysis in hexagonal materials, *Materials Chemistry and Physics*, 81 (2003) 11-26. DOI: [https://doi.org/10.1016/S0254-0584\(03\)00168-8](https://doi.org/10.1016/S0254-0584(03)00168-8).

[67] L.W.F. Mackenzie, B. Davis, F.J. Humphreys, G.W. Lorimer, The deformation, recrystallisation and texture of three magnesium alloy extrusions, *Materials Science and Technology*, 23 (2007) 1173-1180. DOI: 10.1179/174328407X226509.

[68] E.A. Ball, P.B. Prangnell, Tensile-compressive yield asymmetries in high strength wrought magnesium alloys, *Scripta Metallurgica et Materialia*, 31 (1994) 111-116. DOI: [https://doi.org/10.1016/0956-716X\(94\)90159-7](https://doi.org/10.1016/0956-716X(94)90159-7).

[69] J. Bohlen, M.R. Nürnberg, J.W. Senn, D. Letzig, S.R. Agnew, The texture and anisotropy of magnesium–zinc–rare earth alloy sheets, *Acta Materialia*, 55 (2007) 2101-2112. DOI: <https://doi.org/10.1016/j.actamat.2006.11.013>.

[70] M.T. Pérez-Prado, O.A. Ruano, Texture evolution during grain growth in annealed MG AZ61 alloy, *Scripta Materialia*, 48 (2003) 59-64. DOI: [https://doi.org/10.1016/S1359-6462\(02\)00346-9](https://doi.org/10.1016/S1359-6462(02)00346-9).

[71] G.L. Song, A. Atrens, Corrosion Mechanisms of Magnesium Alloys, *Advanced Engineering Materials*, 1 (1999) 11-33. DOI: 10.1002/(sici)1527-2648(199909)1:1<11::aid-adem11>3.0.co;2-n.

[72] B.R. Sunil, A.A. Kumar, T.S. Sampath Kumar, U. Chakkingal, Role of biomineralization on the degradation of fine grained AZ31 magnesium alloy processed by groove pressing,

Materials Science and Engineering: C, 33 (2013) 1607-1615. DOI: <https://doi.org/10.1016/j.msec.2012.12.095>.

[73] B. Ratna Sunil, T.S. Sampath Kumar, U. Chakkingal, V. Nandakumar, M. Doble, V. Devi Prasad, M. Raghunath, In vitro and in vivo studies of biodegradable fine grained AZ31 magnesium alloy produced by equal channel angular pressing, Materials Science and Engineering: C, 59 (2016) 356-367. DOI: <https://doi.org/10.1016/j.msec.2015.10.028>.

[74] D.R. Lopes, C.L.P. Silva, R.B. Soares, P.H.R. Pereira, A.C. Oliveira, R.B. Figueiredo, T.G. Langdon, V.F.C. Lins, Cytotoxicity and Corrosion Behavior of Magnesium and Magnesium Alloys in Hank's Solution after Processing by High-Pressure Torsion, Advanced Engineering Materials, 21 (2019) 1900391. DOI: 10.1002/adem.201900391.

[75] H.-y. Niu, K.-k. Deng, K.-b. Nie, C.-j. Wang, W. Liang, Y.-c. Wu, Degradation behavior of Mg-4Zn-2Ni alloy with high strength and high degradation rate, Materials Chemistry and Physics, 249 (2020) 123131. DOI: <https://doi.org/10.1016/j.matchemphys.2020.123131>.

[76] C.L.P. Silva, R.B. Soares, P.H.R. Pereira, R.B. Figueiredo, V.F.C. Lins, T.G. Langdon, The Effect of High-Pressure Torsion on Microstructure, Hardness and Corrosion Behavior for Pure Magnesium and Different Magnesium Alloys, Advanced Engineering Materials, 21 (2019) 1801081. DOI: 10.1002/adem.201801081.

[77] E. Aghion, G. Golub, Production Technologies of Magnesium, Magnesium Technology: Metallurgy, Design Data, Applications, Springer Berlin Heidelberg, Berlin, Heidelberg, 2006, pp. 29-62.

[78] A. Kocijan, A comparison of the corrosion behaviour of austenitic stainless steels in artificial seawater, Materiali in Tehnologije, 45 (2011) 91-94.

[79] Y. Luo, Y. Deng, L. Guan, L. Ye, X. Guo, A. Luo, Effect of grain size and crystal orientation on the corrosion behavior of as-extruded Mg-6Gd-2Y-0.2Zr alloy, Corrosion Science, 164 (2020) 108338. DOI: <https://doi.org/10.1016/j.corsci.2019.108338>.

[80] R. Xin, B. Li, L. Li, Q. Liu, Influence of texture on corrosion rate of AZ31 Mg alloy in 3.5wt.% NaCl, Materials & Design, 32 (2011) 4548-4552. DOI: <https://doi.org/10.1016/j.matdes.2011.04.031>.

Figure caption

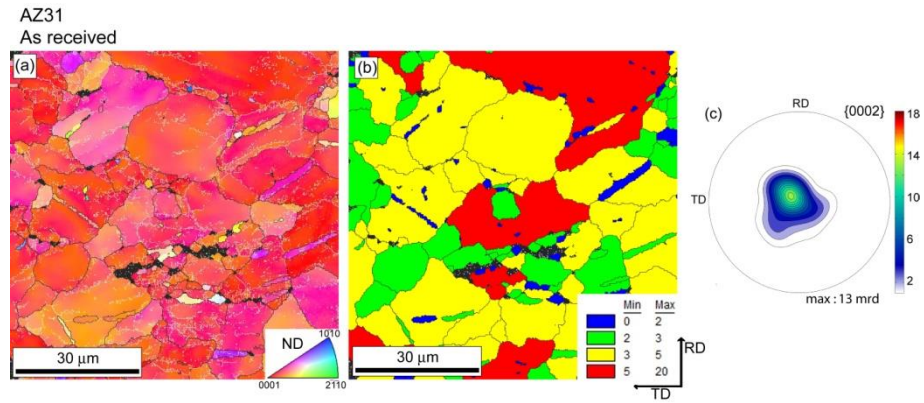


Fig. 1. (a) ND-IPF map, (b) GOS map and (c) recalculated basal $\{0002\}$ pole figure of the as-received AZ31 alloy.

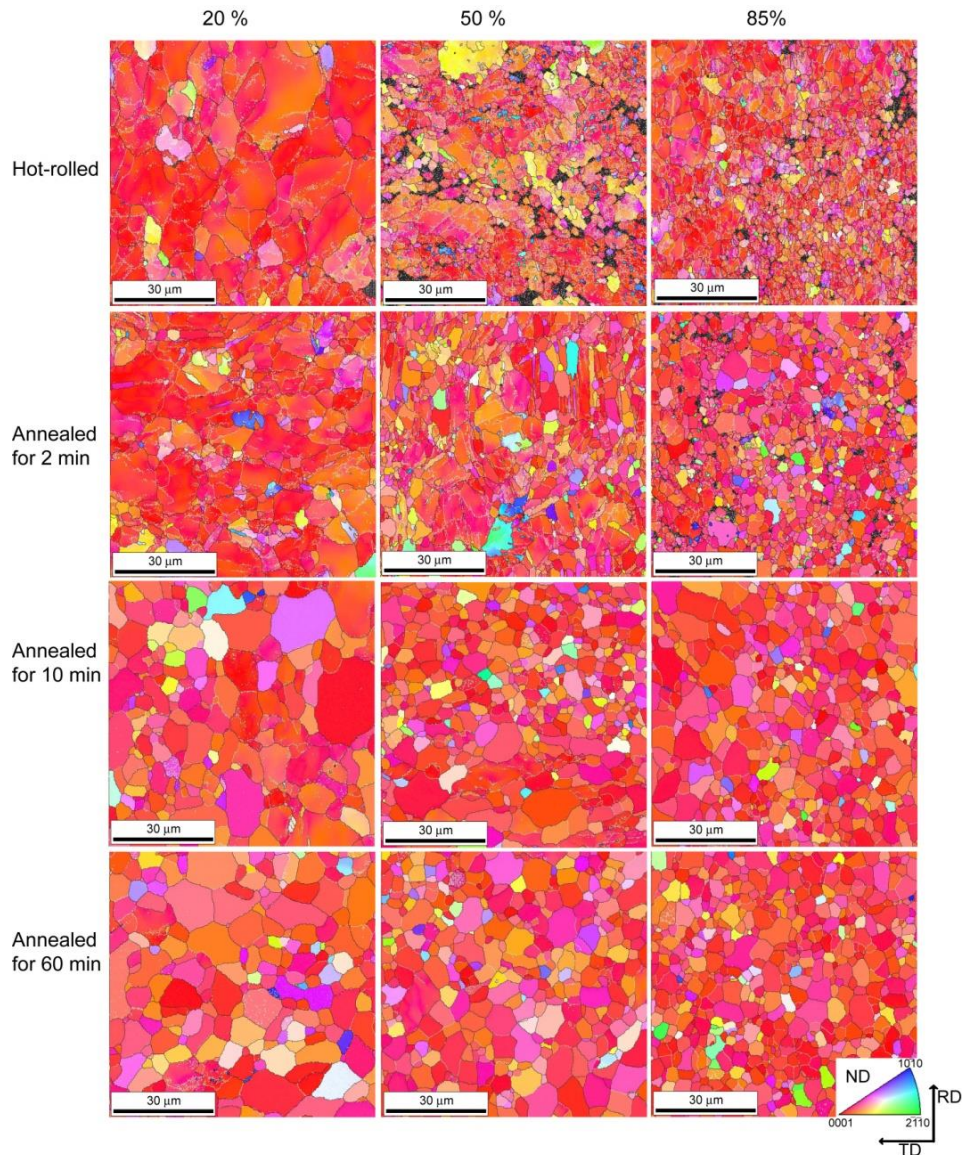


Fig. 2. ND-IPF map of the AZ31 alloy after hot rolling to 20, 50 and 85 % and annealing at 350 °C for 2, 10 and 60 min, respectively.

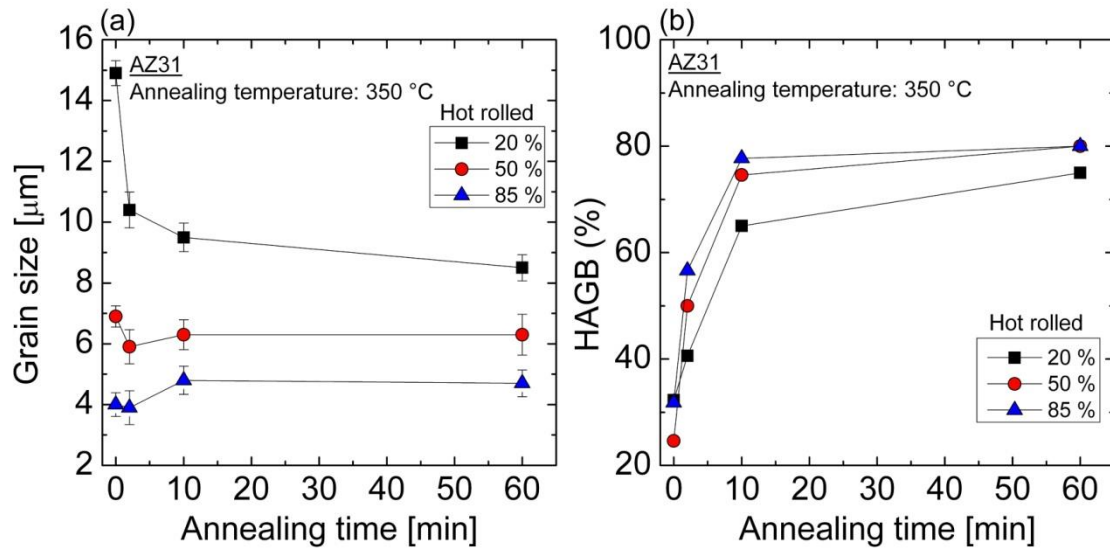


Fig. 3. Evolution of grain size and fraction of high angle grain boundaries as a function of annealing time of the hot-rolled AZ31 alloy at 20, 50 and 85 % of thickness reduction, respectively.

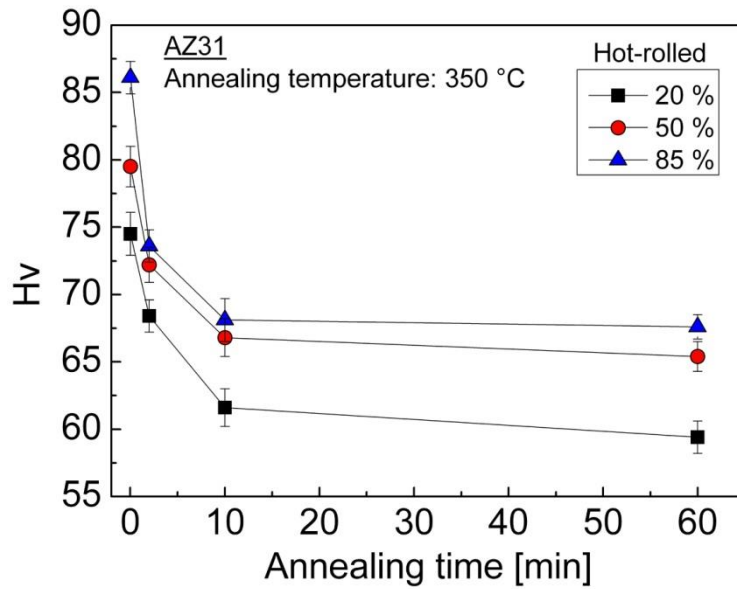


Fig. 4. Evolution of microhardness as a function of annealing time of the hot-rolled AZ31 alloy at 20, 50 and 85 % of thickness reduction, respectively.

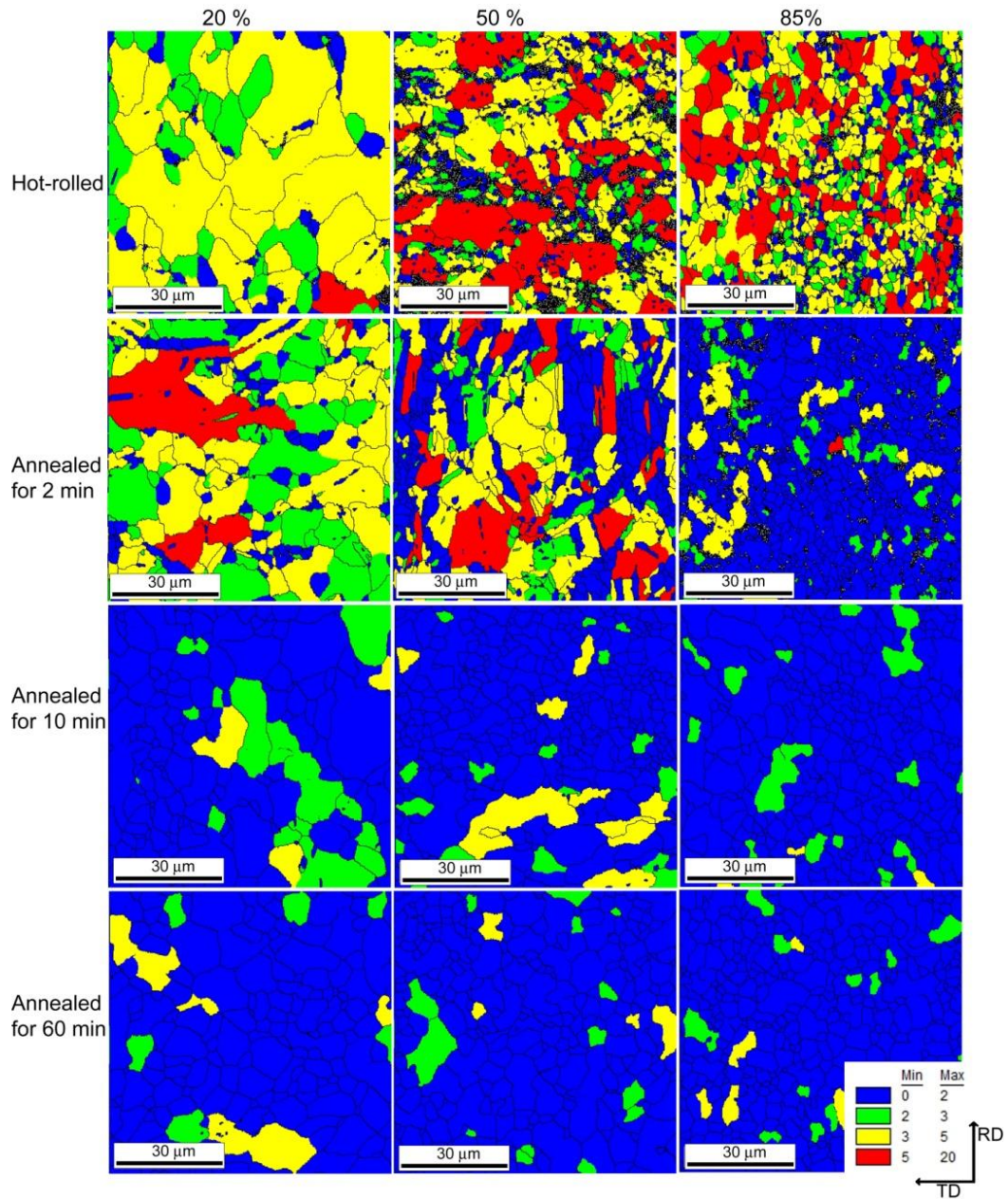


Fig. 5. GOS maps of the hot-rolled AZ31 alloy at 20, 50 and 85 % of thickness reduction and annealing at 350 °C for 2, 10 and 60 min, respectively.

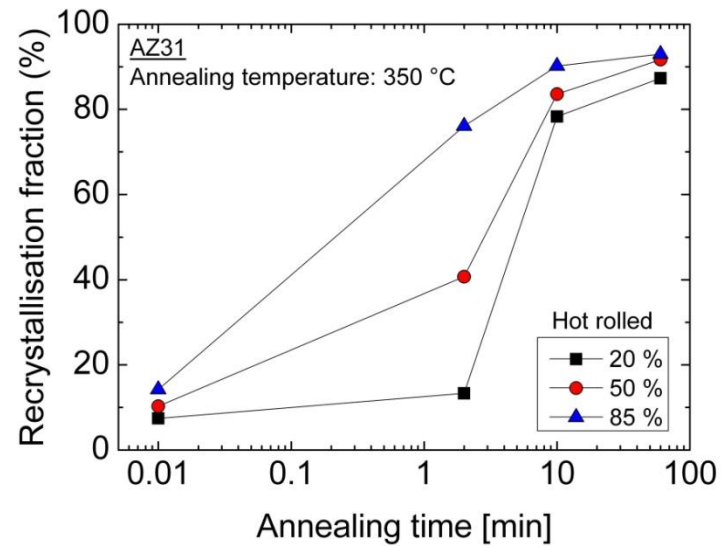


Fig. 6. Evolution of the recrystallisation fraction as a function of annealing time of the hot-rolled AZ31 alloy at 20, 50 and 85 % of thickness reduction, respectively.

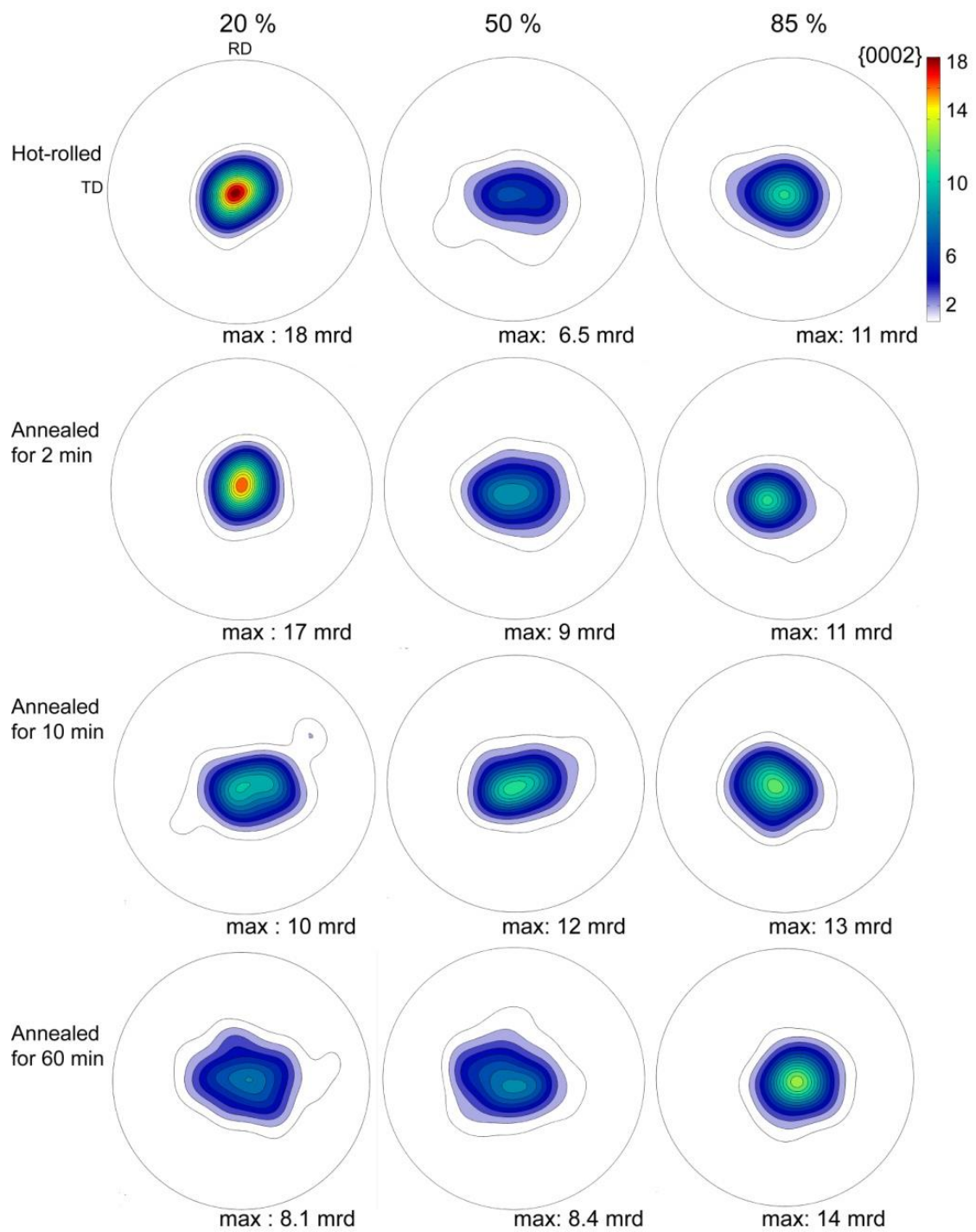


Fig. 7. Recalculated basal {0002} pole figure of the hot-rolled and the annealed AZ31 alloy.

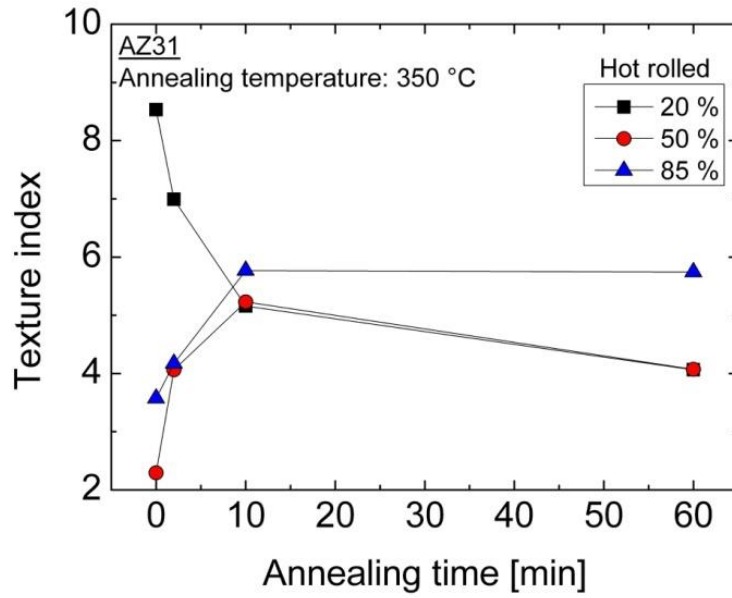


Fig. 8. Evolution of the texture index as a function of annealing time of the hot-rolled and the annealed AZ31 alloy.

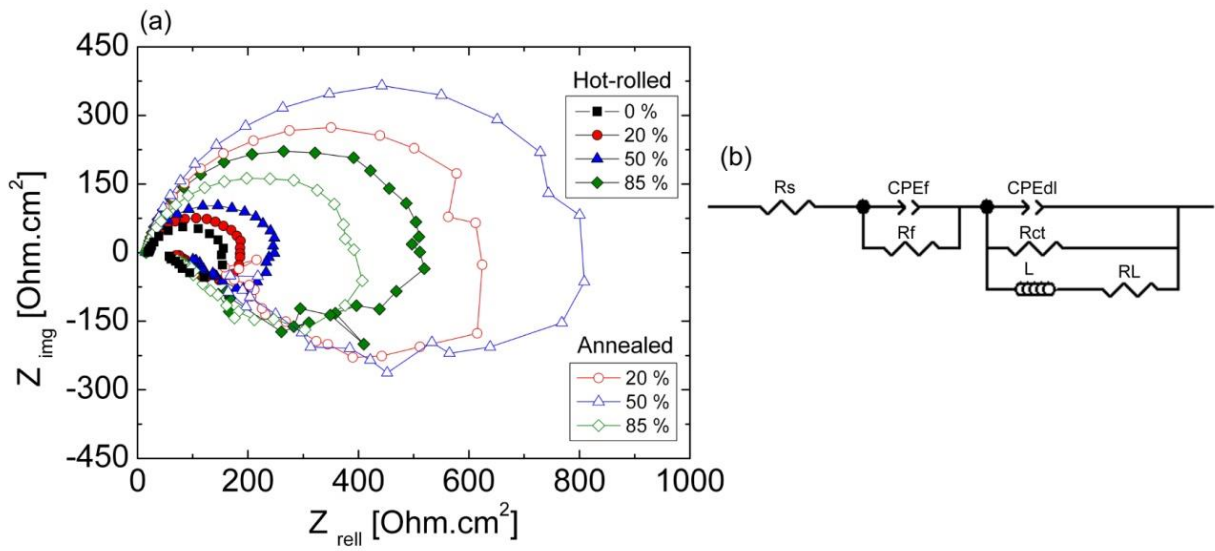


Fig. 9. (a) Nyquist plots and (b) the equivalent circuit of the as-received, hot-rolled and annealed AZ31 alloy in seawater.

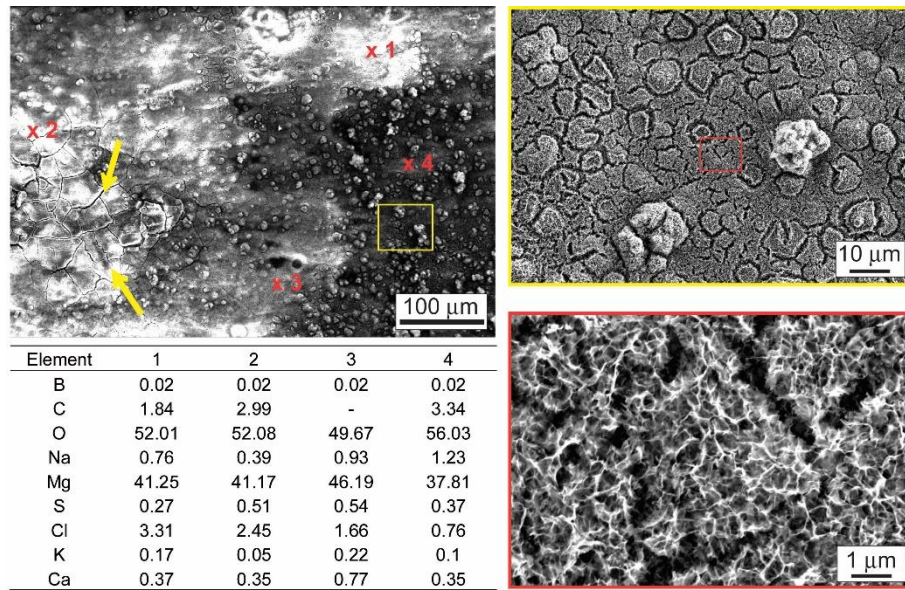


Fig. 10. SEM micrograph with different resolutions and the corresponding EDS analysis in weight percentage of the as-received AZ31 alloy after immersion in seawater for 3 h.

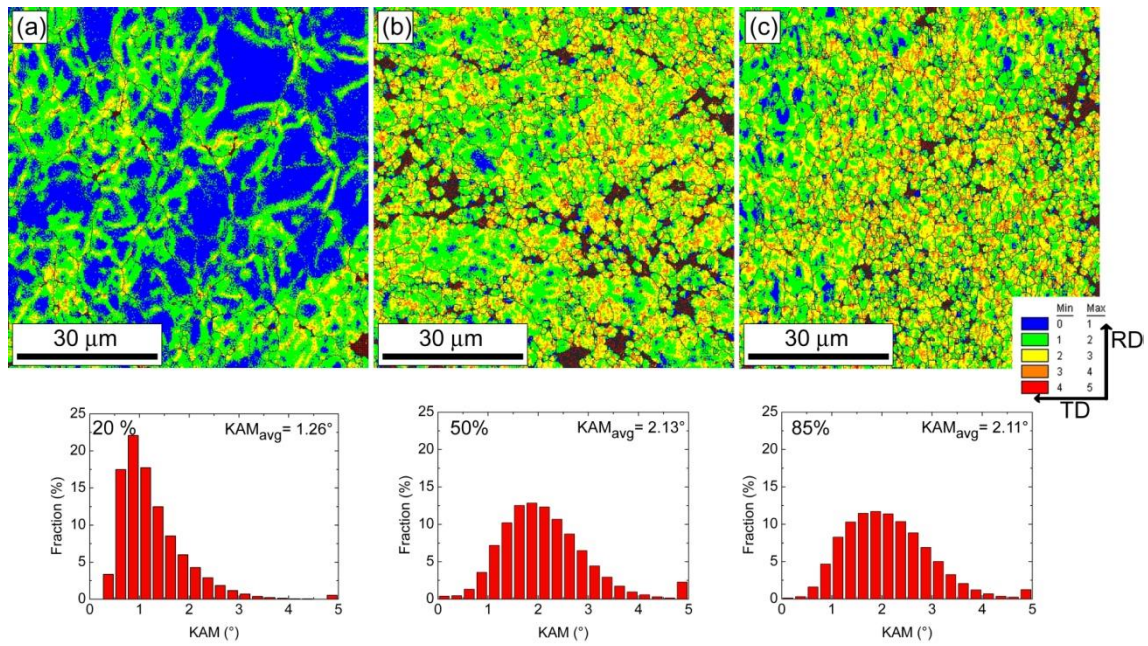


Fig. 11. KAM maps and their corresponding distributions of the hot-rolled AZ31 alloy for 20, 50 and 85 % of thickness reduction, respectively.

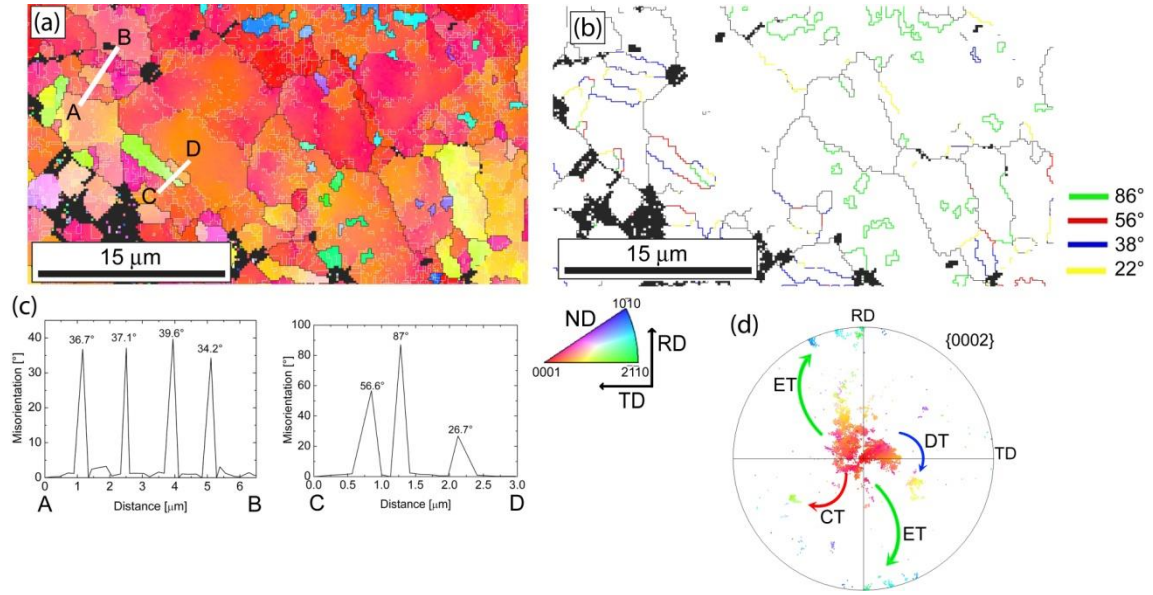


Fig. 12. (a) ND-IPF map of selected region of the 50 % hot-rolled sample, (b) map showing the different twins, (c) misorientation profile along segments from A to B and C to D and (d) the corresponding $\{0002\}$ pole figure indicates the orientation between grains and twins. ET, CT and DT correspond to extension, contraction and double twins, respectively.

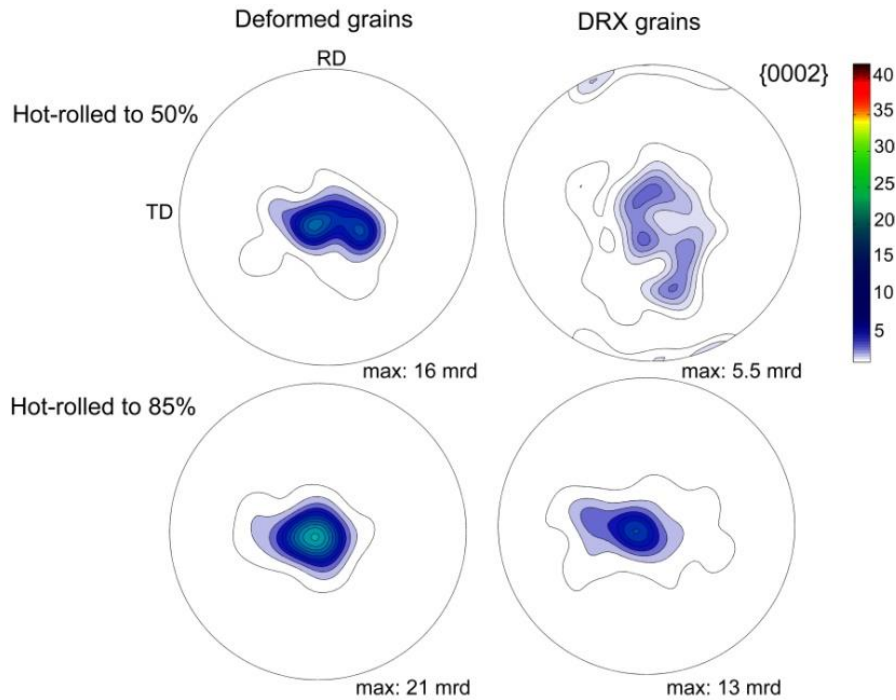


Fig. 13. Recalculated $\{0002\}$ pole figure for the deformed and dynamically recrystallised grains of the 50 and 85 % hot-rolled samples, respectively.

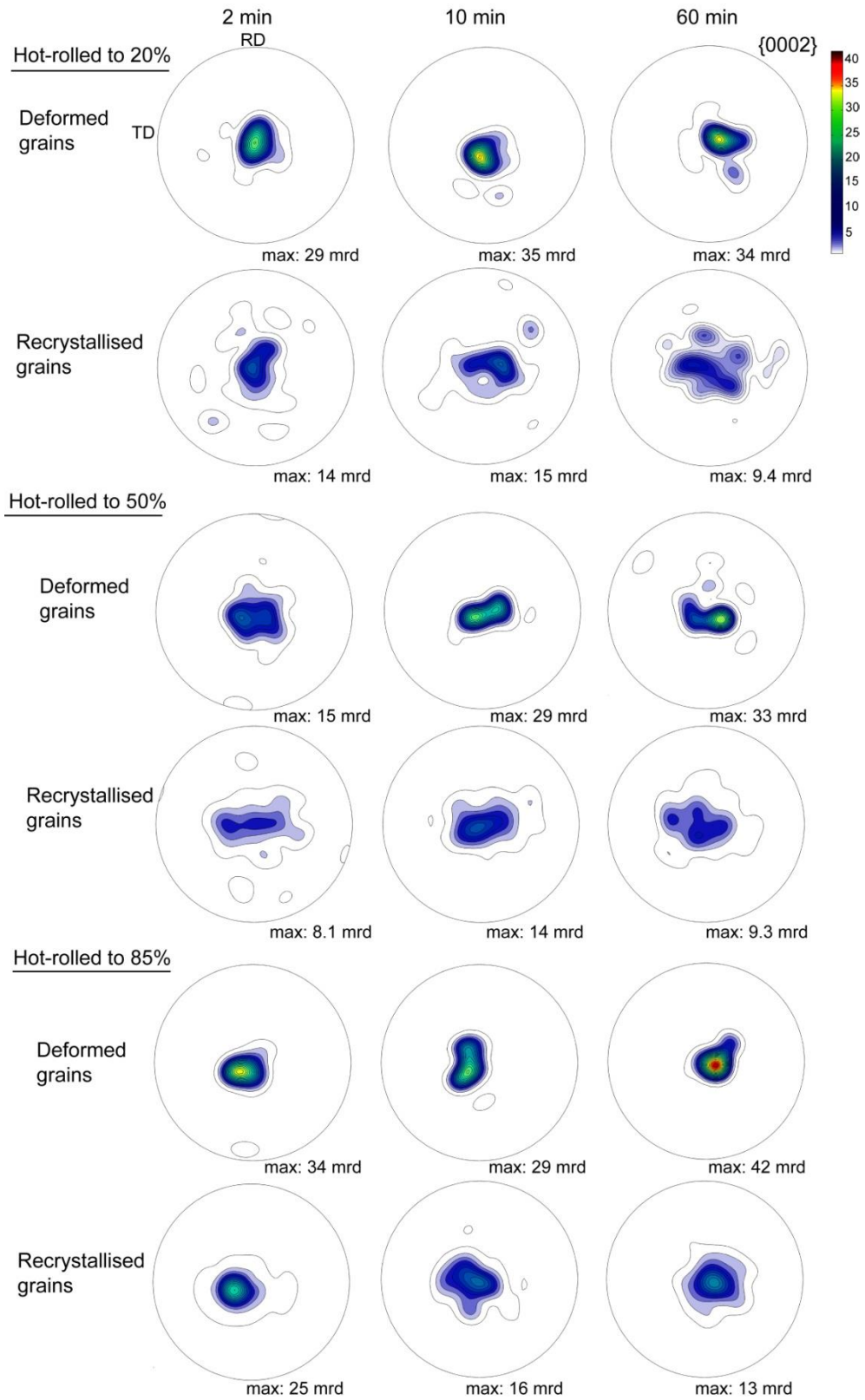


Fig. 14. Recalculated $\{0002\}$ pole figure for the deformed and recrystallised grains as a function of annealing time of the hot-rolled AZ31 alloy for 20, 50 and 85 % of thickness reduction.

Table caption**Table 1.** Chemical composition of AZ31 alloy.

Al	Zn	Mn	Ca	Cu	Fe	Mg
3.45	0.98	0.28	0.002	0.002	0.004	Balance

Table 2. Electrochemical parameters obtained from the fits of the experimental Nyquist data of the AZ31 samples in seawater.

	R_s ($\Omega\cdot\text{cm}^2$)	CPE_f ($\text{F}\cdot\text{cm}^{-2}$)	R_f ($\Omega\cdot\text{cm}^2$)	CPE_{dl} ($\text{F}\cdot\text{cm}^{-2}$)	R_{ct} ($\Omega\cdot\text{cm}^2$)	L ($\text{H}\cdot\text{cm}^{-2}$)	R_L ($\Omega\cdot\text{cm}^2$)	R_p ($\Omega\cdot\text{cm}^2$)
		$Y (\times 10^{-4})$	n	$Y (\times 10^{-5})$	n			
<u>Hot-rolled</u>								
0%	18.04	16	0.48	3.12	8.4	0.87	137.8	76.31
20%	11.96	7	0.31	5.4	8.45	0.89	176.8	109.08
50%	16.55	100	0.35	6.88	5.07	0.98	230.8	161.02
85%	14.7	40	0.39	8.51	2.8	0.95	466.3	174.84
<u>Annealed</u>								
20%	13.79	1.9	0.52	15.17	4.27	0.92	611.2	223.62
50%	14.55	1.9	0.6	64.98	4.03	0.96	710.2	264.13
85%	14.21	21	0.5	7.38	4.96	0.91	376.7	96.92

Table 3. Fraction (F) of different twins identified in the hot-rolled samples (from Fig. 2).

Twin mode	Misorientation (Angle/Axis)	F (%)		
		20 %	50 %	85 %
$\{10\bar{1}2\}$ extension twin	$86^\circ \pm 8^\circ \langle 11\bar{2}0 \rangle$	1.8	5.1	1.5
$\{10\bar{1}1\}$ contraction twin	$56^\circ \pm 8^\circ \langle 11\bar{2}0 \rangle$	1.1	1.3	1.5
$\{10\bar{1}1\}\{10\bar{1}2\}$ double twin	$38^\circ \pm 8^\circ \langle 11\bar{2}0 \rangle$	1.4	2.4	1.7
$\{10\bar{1}3\}\{10\bar{1}2\}$ double twin	$22^\circ \pm 8^\circ \langle 11\bar{2}0 \rangle$	1.1	2.0	3.4